T2R2 東京科学大学 リサーチリポジトリ
Science Tokyo Research Repository

# 論文 / 著書情報
# Article / Book Information

| | |
|---|---|
| Title | Chemical Trends of Surface Reconstruction and Band Positions of Nonmetallic Perovskite Oxides from First Principles |
| Authors | Yasuhide Mochizuki, Ha-Jun Sung, Tomoya Gake, Fumiyasu Oba |
| Citation | Chemistry of Materials, Vol. 35, Issue 5, pp. 2047-2057 |
| Pub. date | 2023, 2 |
| DOI | https://doi.org/10.1021/acs.chemmater.2c03615 |
| Creative Commons | Information is in the article. |

Powered by T2R2 (Science Tokyo Research Repository)

CHEMISTRY OF MATERIALS

pubs.acs.org/cm

Article

# Chemical Trends of Surface Reconstruction and Band Positions of Nonmetallic Perovskite Oxides from First Principles

Yasuhide Mochizuki,* Ha-Jun Sung, Tomoya Gake, and Fumiyasu Oba*

Cite This: *Chem. Mater.* 2023, 35, 2047−2057

Read Online

ACCESS | Metrics & More | Article Recommendations | Supporting Information

**ABSTRACT:** An evolutionary algorithm search in combination with first-principles calculations is performed to systematically predict the reconstructed surface structures of nonmetallic perovskite oxides. Four types of lowest-energy reconstruction patterns are obtained for the macroscopically stoichiometric (001) surfaces of $NaTaO_3$, $KTaO_3$, $CaTiO_3$, $SrTiO_3$, $YAlO_3$, and $LaAlO_3$ as representatives of $A^+B^{5+}O_3$, $A^{2+}B^{4+}O_3$, and $A^{3+}B^{3+}O_3$ systems. We explain chemical trends in the surface energies and band positions of 10 perovskite oxides, additionally including $KNbO_3$, $BaTiO_3$, $BaZrO_3$, and $LaGaO_3$, in terms of the atomic environments at the outermost reconstructed surface layers. Regaining $A$−O ($B$−O) coordination numbers and bond lengths at the surfaces is found to stabilize the $A^{2+}B^{4+}O_3$ and $A^{3+}B^{3+}O_3$ ($A^+B^{5+}O_3$) surfaces. Decreasing the coordination number of cation $A$ ($B$) leads to shallow (deep) valence band maxima and conduction band minima relative to the vacuum level. Our study provides general insights into the surface reconstruction and band alignment of nonmetallic perovskite oxides.

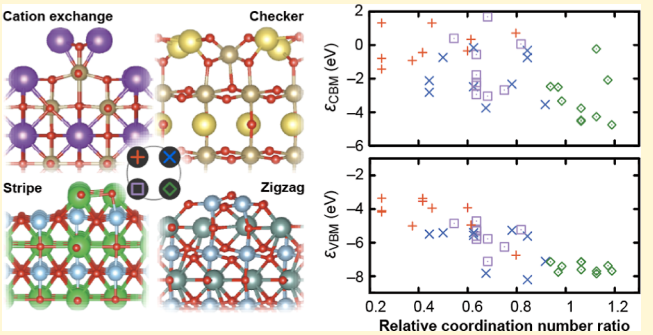


Downloaded via TOKYO INST OF TECHNOLOGY on March 14, 2023 at 08:21:02 (UTC).
See https://pubs.acs.org/sharingguidelines for options on how to legitimately share published articles.

## 1. INTRODUCTION

A tremendous amount of research has been devoted to perovskite oxides because of their versatile physical and chemical properties such as ferroelectricity,[1−16] antiferroelectricity,[17−19] ferromagnetism,[15,16,20,21] multiferroicity,[22,23] quantum paraelectricity,[24−27] superconductivity,[28−35] metal−insulator transition,[36−43] two-dimensional electron gas formation,[44,45] catalysis,[46−52] and photocatalysis.[53−56] These fascinating properties of perovskite oxides are widely tunable by utilizing their high flexibility in the structural distortion,[7−14,36−39,57−59] chemical composition,[6−8,29−34] doping,[29,42,43] epitaxial strain modulation,[1−4,22,23,60] and superlattice fabrication.[5,44,45] This feature offers great advantages in the design and optimization of diverse applications using perovskite oxides.

The energy band position relative to the vacuum level or the band position of another material is fundamental and essential information to design surfaces and heterointerfaces in electronic, electrochemical, and photocatalytic applications.[61−64] The band alignment of surfaces, namely, the lineup of their electron affinities (EAs) and ionization potentials (IPs), depends on the polymorphism, surface structure, stoichiometry, polarity, and various environmental conditions through the change in the surface dipole contribution.[63−74] For instance, a first-principles study by Buckeridge et al. indicates that the EAs and IPs of $TiO_2$ can be tuned over a 4 eV range by controlling its polymorphism and surface orientation.[65] Furthermore, the theoretically reported band positions of the fully $AO$- and $BO_2$-terminated surfaces of $A^{2+}B^{4+}O_3$ perovskites are considerably different from each other.[63,66] A recent experimental study by Thapa et al. has shown that $SrTiO_3$ surfaces exhibit a mixture of the SrO and $TiO_2$ terminations or a full SrO termination during the hybrid oxide molecular beam epitaxy growth of stoichiometric films on $SrTiO_3$ (001) single crystal substrates.[75] Our previous first-principles calculations have predicted that the band positions of reconstructed $SrTiO_3$ (001) surfaces with mixed terminations show up to ∼1 eV differences from those of fully SrO- and $TiO_2$-terminated surfaces.[66] Such theoretical investigation into reconstructed surface structures and band positions has hitherto been limited mostly to prototypical systems such as $SrTiO_3$, $BaTiO_3$, and $KTaO_3$.[63,76−79] Thus, systematically modeling the reconstructed surfaces of remaining $ABO_3$ and understanding the chemical tendency are pressing issues.

In this study, we focus on the extensively studied representative (001) surfaces of perovskite oxides and perform first-principles calculations to investigate their reconstructed structures, stability, and band positions. Based on a hybrid functional approach, we evaluate the chemical trends in the surface energies, EAs, and IPs of 10 nonmetallic perovskites

Received: December 3, 2022
Revised: February 6, 2023
Published: February 21, 2023

ACS Publications

© 2023 American Chemical Society

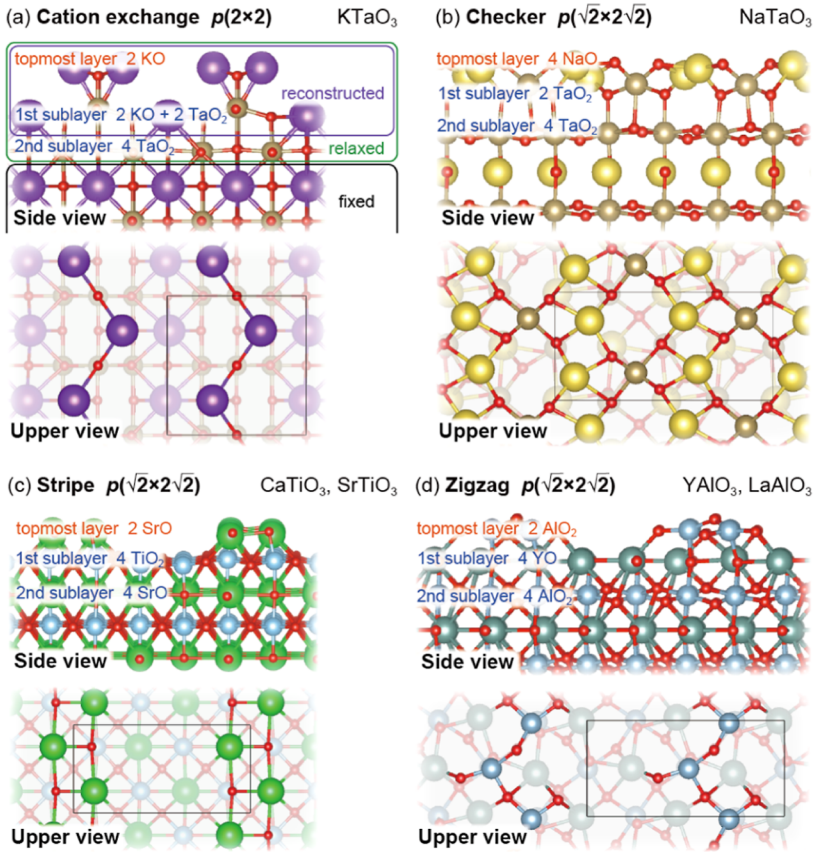


**Figure 1.** Four reconstructed surface structures for $A^{+}B^{5+}O_3$, $A^{2+}B^{4+}O_3$, and $A^{3+}B^{3+}O_3$, which are denoted (a) cation-exchange, (b) checker, (c) stripe, and (d) zigzag models. The solid lines in the upper view indicate the surface periodicity units; the notations of $p(2 \times 2)$ and $p(\sqrt{2} \times 2\sqrt{2})$ are based on a pseudo-cubic representation. See Computational Methods for the reconstructed, relaxed, and fixed regions of the surface models indicated in (a).

$A^{+}B^{5+}O_3$, $A^{2+}B^{4+}O_3$, and $A^{3+}B^{3+}O_3$ using prototypical reconstructed structure models for macroscopically nonpolar and stoichiometric (001) surfaces derived by an evolutionary algorithm search.

## 2. RESULTS AND DISCUSSION

**2.1. Surface Reconstruction, Energy, and Band Position.** It is known that about 90% of the perovskite oxides have one of the 6 octahedral-distorted structures, the space-group symmetries of which are $Im\bar{3}$ ($a^{+}a^{+}a^{+}$), $R\bar{3}c$ ($a^{-}a^{-}a^{-}$), $I4/mcm$ ($a^{0}b^{0}c^{-}$), $P4/mbm$ ($a^{0}b^{0}c^{+}$), $Ibmm$ ($a^{-}a^{-}c^{0}$), and $Pbnm$ ($a^{-}a^{-}c^{+}$).[80] Among the 7 polymorphs additionally including the undistorted cubic phase ($Pm\bar{3}m$), we found that the $Pbnm$ phase is the most stable in $CaTiO_3$, $NaTaO_3$, $YAlO_3$, and $LaGaO_3$, while the cubic phase is the most stable in $BaTiO_3$, $KNbO_3$, and $KTaO_3$. On one hand, in $SrTiO_3$ and $LaAlO_3$, the most stable phases were found to be the $I4/mcm$ and $R\bar{3}c$ phases, respectively (see Figure S1 in the Supporting Information for the calculation results of the 7 phases for the 10 perovskite oxides and the note on the polar $R3m$ phase of $BaTiO_3$ and $KNbO_3$). We adopted the $Pbnm$ phase for $CaTiO_3$, $NaTaO_3$, $YAlO_3$, $LaAlO_3$, and $LaGaO_3$ and the $Pm\bar{3}m$ phase for $SrTiO_3$, $BaTiO_3$, $BaZrO_3$, $KNbO_3$, and $KTaO_3$ in the surface calculations to reduce the complexity associated with the structural distortion; our previous study has shown that the surface reconstruction patterns are quite similar to each other for the $I4/mcm$ and $Pm\bar{3}m$ phases of $SrTiO_3$.[66]

Our evolutionary algorithm search derived 4 types of lowest-energy reconstruction patterns: the *cation-exchange*, *checker*, *stripe*, and *zigzag* structures are obtained for $NaTaO_3$, $KTaO_3$, $CaTiO_3$, $SrTiO_3$, $YAlO_3$, and $LaAlO_3$ as illustrated in Figure 1a–d (see the Supporting Information for the crystallographic data). The cation-exchange structure is essentially identical to the previously reported $KTaO_3$ surface model by Deacon-Smith et al., where the topmost layer and the first sublayer are completely reconstructed from an ideally cleaved surface with the half-$BO_2$ topmost layer (2 $TaO_2$ in unit surface area) and the full-$AO$ first sublayer (4 KO in unit surface area) so that cations $A$ and $B$ are exchanged between these layers.[76] The checker structure predicted here also involves cation exchange and has an $AO$ topmost layer and a half-$BO_2$ first sublayer that are very closely located. The stripe structure was reproduced from our previous study on $A^{2+}B^{4+}O_3$ reconstructed surfaces,[66] which also predicted a similar half-$BO_2$-terminated structure to the zigzag structure identified here for $YAlO_3$ and $LaAlO_3$. These stripe and zigzag structures preserve the original stacking sequence of the $AO$ and $BO_2$ layers, and hence, their topmost layers are either half-$AO$- or half-$BO_2$-terminated to conform to stoichiometry. Note that the unreconstructed $ABO_3$ perovskite (001) surfaces that are terminated fully by the $AO$ or $BO_2$ planes are nonstoichiometric and polar (Tasker type 3[81,82]), while our reconstructed surfaces are macroscopically stoichiometric and nonpolar. Previous reports on the $ABO_3$ (001) surfaces have indicated that charge compensation is a key factor for the surface reconstruction, the mechanisms


https://doi.org/10.1021/acs.chemmater.2c03615
Chem. Mater. 2023, 35, 2047−2057

of which include the half-topmost layer termination, cation exchange, and rumpling.[77,83,84]

By using the 4 reconstructed surface models as templates, we relaxed the structures and calculated their surface energies in 10 $ABO_3$ perovskites. The surface energy $E_{surf}$ is given as

$$E_{surf} = \frac{1}{2S}(E_{slab} - NE_{ABO_3}) \quad (1)$$

where $E_{slab}$ and $E_{ABO_3}$ are, respectively, the total energy of a slab model with reconstructed surfaces on both sides and the total energy per formula unit for bulk $ABO_3$. $N$ is the number of the $ABO_3$ formula unit in the slab model. $S$ is the $ab$-plane unit surface area, and the factor of 2 is due to the presence of two identical surfaces in the slab model. From Figure 2a, we can see a chemical trend that the stripe or zigzag structure is energetically the most favorable in $A^{2+}B^{4+}O_3$ and $A^{3+}B^{3+}O_3$, whereas the cation-exchange or checker structure is slightly preferable in $A^{+}B^{5+}O_3$.

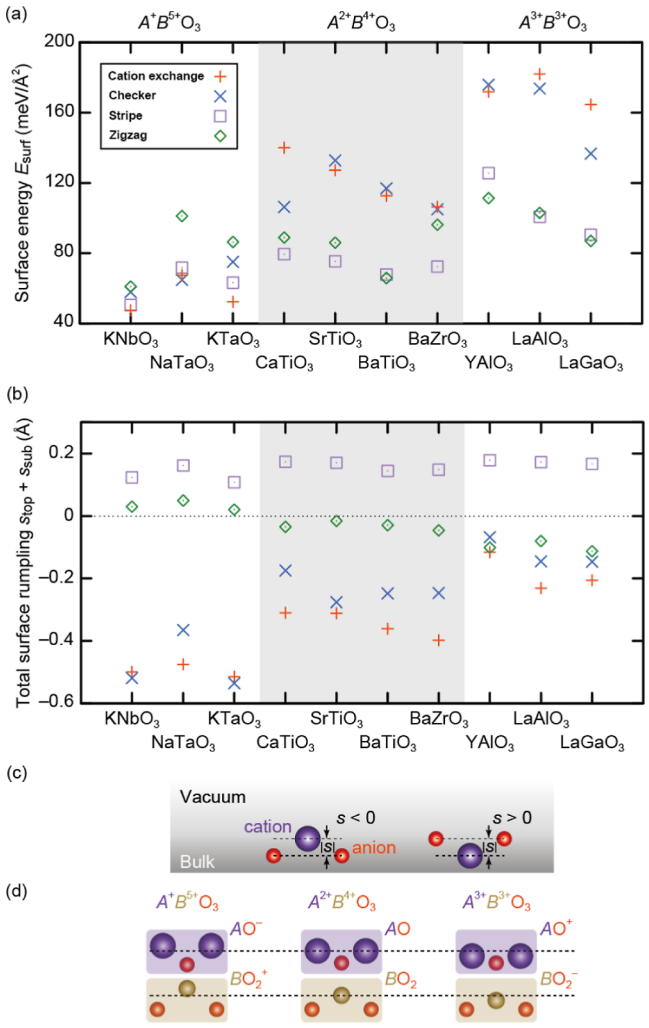


**Figure 2.** (a) Surface energies and (b) total surface rumpling for $A^+B^{5+}O_3$, $A^{2+}B^{4+}O_3$, and $A^{3+}B^{3+}O_3$. In the case where anions (cations) are closer to the vacuum region on average, the total surface rumpling is defined to be positive (negative), as illustrated in (c). (d) Schematics of the atomic positions in the half-$AO$ topmost layer and a $BO_2$ region in the $AO-BO_2$ mixed first sublayer under the topmost layer in the cation-exchange surface structure for $A^+B^{5+}O_3$, $A^{2+}B^{4+}O_3$, and $A^{3+}B^{3+}O_3$.

Figure 2b shows the degree of surface rumpling in the 4 reconstructed surface structures. We calculated the total surface rumpling on the topmost layers ($s_{top}$) and first sublayers ($s_{sub}$), which are defined to be positive (negative) when anions (cations) are closer to the vacuum region as illustrated in Figure 2c. The cation-exchange and checker structures exhibit relatively large and negative surface rumpling, which corresponds to the outward average displacement of the cations on the topmost layer and the first sublayer. On the other hand, positive and nearly zero total rumpling with much smaller composition dependencies is found in the stripe and zigzag structures, respectively. Positive surface-rumpling behavior has experimentally been observed in stoichiometric nonpolar rock-salt (001) surfaces of NaCl and KCl,[85] which are categorized as Tasker type 1.[81,82] A recent first-principles study by Hinuma et al. has shown that the (001) surfaces of rock-salt oxides tend to have positive (negative) $s_{top}$ when the cationic radius is small (large).[73] In the present case of the perovskite surfaces, the negative total rumpling of the cation-exchange and checker structures could be attributed to the charge compensation in addition to the size effect. We can see that the norms of the total rumpling of the cation-exchange and checker structures for $A^+B^{5+}O_3$ and $A^{3+}B^{3+}O_3$ are, respectively, larger and smaller than those for $A^{2+}B^{4+}O_3$ (see the plus and cross marks in Figure 2b). To explain such rumpling behavior concisely, the half-$AO$ topmost layer and a $BO_2$ region in the $AO-BO_2$ mixed first sublayer in the cation-exchange structure are illustrated in Figure 2d. Both $AO$ and $BO_2$ layers are formally neutral in $A^{2+}B^{4+}O_3$, while their formal charges are, respectively, −1 and +1 (+1 and −1) in $A^+B^{5+}O_3$ ($A^{3+}B^{3+}O_3$). Cation $A$ on the topmost layer is affected by a repulsive (attractive) force from the $BO_2^+$ ($BO_2^-$) region beneath. Cation $B$ in the $BO_2^+$ ($BO_2^-$) region of the first sublayer is affected by an attractive (repulsive) force from $AO^-$ ($AO^+$) and cation $A$ on the first sublayer as well. The second sublayer is fully composed of $BO_2^+$ ($BO_2^-$) and interacts repulsively (attractively) with the cations on the topmost layer and the first sublayer. A similar discussion holds for the checker structures, explaining the larger and smaller total rumpling in $A^+B^{5+}O_3$ and $A^{3+}B^{3+}O_3$ than that in $A^{2+}B^{4+}O_3$, respectively, as in the case of the cation-exchange structures.

Turning to the electronic structure, the band gaps of the 10 perovskite oxides considered in this study are generally well reproduced, as summarized in Table 1. To clarify the trend, the calculated band gaps are shown as a function of the lattice

**Table 1. Calculated and Experimental Band Gaps of 10 Perovskite Oxides in the Unit of eV[a]**

| compound | band gap (calc) | band gap (exp) |
|---|---|---|
| $CaTiO_3$ | 3.57 | 3.58[93] |
| $SrTiO_3$ | 3.07 | 3.25[94] |
| $BaTiO_3$ | 2.93 | 3.20[90] |
| $BaZrO_3$ | 4.68 | 5.30[95] |
| $YAlO_3$ | 7.46 | 7.85[96] |
| $LaAlO_3$ | 5.25 | 5.6[62] |
| $LaGaO_3$ | 5.29 | 4.4[97] |
| $KNbO_3$ | 2.67 | 3.23[98] |
| $NaTaO_3$ | 4.08 | 4.1[99] |
| $KTaO_3$ | 3.38 | 3.6[99] |

[a]The experimental values are taken from refs 62, 90, and 93−99.


https://doi.org/10.1021/acs.chemmater.2c03615
Chem. Mater. 2023, 35, 2047−2057

constant in Figure 3. It is known that the conduction band minimum (CBM) and valence band maximum (VBM) of

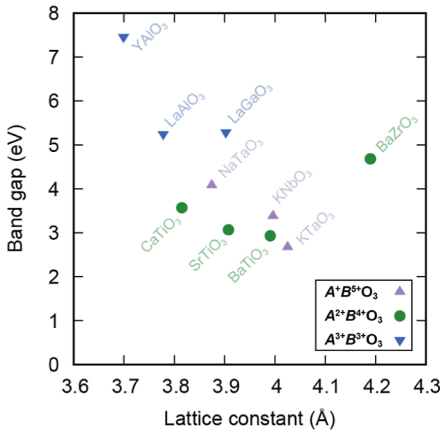


**Figure 3.** Calculated band gaps for 10 perovskite oxides as a function of the lattice constant.

$ABO_3$ are mainly composed of *A*- or *B*-d states and O-2p states, respectively.[96,100,101] Among isostructural and isovalent crystals, smaller constituent ions tend to yield larger band gaps in a simple ionic picture because of greater effects of Madelung potential, the trend of which is almost the same for the perovskite oxides as shown in Figure 3. However, there is an exception: the band gap of $BaZrO_3$ is larger than that of $CaTiO_3$, $SrTiO_3$, and $BaTiO_3$ despite its larger lattice constant. This phenomenon might be attributed to strong covalent interactions between Zr-4d and O-2p states.

The calculated EAs and IPs for the 4 reconstructed surfaces are shown in Figure 4a–d. The EA and IP, respectively, are the negative values of the CBM and VBM with respect to the vacuum level. Hereafter, we use $\varepsilon_{CBM}$ and $\varepsilon_{VBM}$ as the terms of the CBM and VBM relative to the vacuum level, respectively. Figure 4e,f shows a clear trend that $\varepsilon_{CBM}$ and $\varepsilon_{VBM}$ are relatively shallow in the cation-exchange structures, moderate in the checker and stripe structures, and relatively deep in the zigzag structures. We can get a grasp on the reason for this chemical trend from the previous experimental and theoretical studies on $ABO_3$ surfaces: $\varepsilon_{CBM}$ and $\varepsilon_{VBM}$ tend to be shallower for *A*O-terminated surfaces whereas deeper for $BO_2$-terminated surfaces,[63,66,86] and this tendency holds for the reconstructed stoichiometric surfaces of $A^{2+}B^{4+}O_3$ with half-*A*O- and half-$BO_2$-terminated topmost layers.[66] As illustrated in Figure 1, the topmost layers are *A*O-terminated in the cation-exchange, checker, and stripe structures and $BO_2$-terminated in the zigzag structure. Specifically, 2 *A*O, 4 *A*O, 2 *A*O, and 2 $BO_2$ units can be observed per unit surface area in the respective topmost layers.

Figure 4 also indicates the reported experimental $\varepsilon_{CBM}$ and $\varepsilon_{VBM}$ values.[62,87−92] The detailed structures are unclear for most of the experimentally investigated surfaces, which makes a direct comparison between theory and experiment difficult. For $CaTiO_3$ and $SrTiO_3$, the experimental values show a large spread of more than 1 eV, indicating the sensitivity of the band positions to the surface structures. The shallower and deeper experimental levels are close to our theoretical band edge positions of the most stable stripe and the second most stable zigzag structures, respectively. For the other systems, the experimental band edge positions tend to agree well with the theoretical values for the zigzag structures.

**2.2. Chemical Trends of Surface Energy and Band Position.** To further understand the chemical trends of the surface energies, $\varepsilon_{CBM}$, and $\varepsilon_{VBM}$, we use the following two descriptors: *M*−O coordination numbers *n* and bond lengths *l* for both the surface ($n_{surf}$, $l_{surf}$) and bulk ($n_{bulk}$, $l_{bulk}$). The *n* and *l* are extracted by considering the cutoff radius for each cation (see Table S1, Figure S4, and relevant text in the Supporting Information). For the orthorhombic phases with octahedral distortions, $n_{bulk}$ of the *A*-site cations except La is reduced from the ideal cubic value of 12 to 8 in our definition. In addition, the estimation of $n_{surf}$ considers the outermost layers that contain the corresponding cation species. For instance, in the cation-exchange model of $KTaO_3$, under the respective bond length cutoffs of 3.25 Å and 2.75 Å for K and Ta, $n_{surf}$ of K and Ta is 3 and 6 on the topmost layer and the first sublayer, respectively (see the side view of Figure 1a).

In Figure 5a–f, the surface energies are plotted as a function of $n_{surf}/n_{bulk}$ or $l_{surf}/l_{bulk}$. Note that the further away from 1 these ratios are, the difference from the bulk environment becomes significant in terms of the coordination numbers and bond lengths. In $A^{2+}B^{4+}O_3$ and $A^{3+}B^{3+}O_3$, there is a weak tendency that the surface energies decrease as both $n_{surf}/n_{bulk}$ and $l_{surf}/l_{bulk}$ for the *A*−O bonds are closer to 1. On the other hand, in $A^{+}B^{5+}O_3$, the surface energies tend to lower as both $n_{surf}/n_{bulk}$ and $l_{surf}/l_{bulk}$ for the *B*−O bonds are closer to 1. As seen from these results, the driving force for the surface reconstructions in $A^{2+}B^{4+}O_3$ and $A^{3+}B^{3+}O_3$ ($A^{+}B^{5+}O_3$) would partly be regaining the *A*−O (*B*−O) coordination numbers and bond lengths in the bulk as much as possible. It has previously been reported that the reconstruction of the $KTaO_3$ (001) surface occurs to fulfill the Ta coordination,[76] which is consistent with our insight. We refer here that the correlation between $E_{surf}$ and the *B*−O coordination number or bond length ratio in $A^{2+}B^{4+}O_3$ and $A^{3+}B^{3+}O_3$ is less clear as well as that between $E_{surf}$ and the *A*−O coordination number or bond length ratio in $A^{+}B^{5+}O_3$ (see Figure S2 in the Supporting Information). The different chemical trends in the surface energy among $A^{2+}B^{4+}O_3$, $A^{3+}B^{3+}O_3$, and $A^{+}B^{5+}O_3$ might originate from the flexibility of *A* cations' oxygen coordination environments. For instance, the smallest coordination number of $Na^+$ and $K^+$ is 3 in bulk metal oxides whereas that of $Ca^{2+}$, $Sr^{2+}$, $Ba^{2+}$, $Y^{3+}$, and $La^{3+}$ is larger than 5.[102] Thus, the alkali metal ions in $A^{+}B^{5+}O_3$ perovskites would allow for the small coordination number at the topmost surface layer to make the cation-exchange structure relatively favorable.

To discuss the surface energy from a concise electrostatics viewpoint, we calculated the Madelung surface energy, which is given as

$$E_{surf}^{Madelung} = \frac{1}{2S}\left(E_{slab}^{Madelung} - NE_{ABO_3}^{Madelung}\right) \quad (2)$$

where $E_{slab}^{Madelung}$ and $E_{ABO_3}^{Madelung}$ are the Madelung energy of a slab model and that of a bulk model per $ABO_3$ formula unit, respectively, and *N* and *S* indicate the same as those given in eq 1. As shown in Figure 5g–i, there are positive correlations between $E_{surf}$ and $E_{surf}^{Madelung}$ in all 10 perovskite oxides. These results indicate that lowering the Madelung surface energy is a key factor for the surface reconstruction. Such a simple insight can also be seen in the rock-salt (001) ideal surfaces, which have the lowest Madelung surface energy among ideal nonpolar surfaces with small indices.[103] Taken together with all discussions of the surface energy, the


https://doi.org/10.1021/acs.chemmater.2c03615
Chem. Mater. 2023, 35, 2047−2057

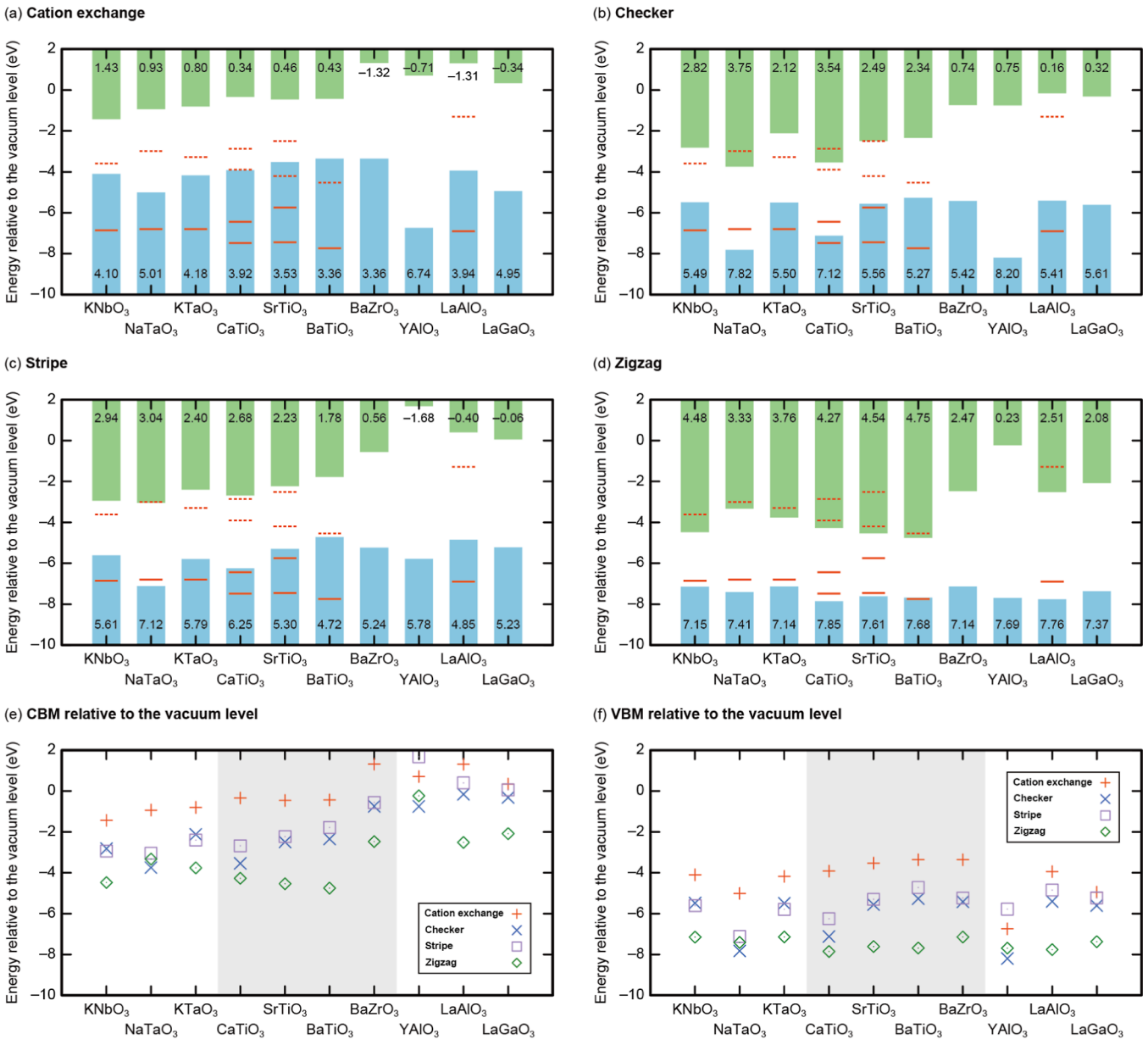


**Figure 4.** Band alignments of (a) cation-exchange, (b) checker, (c) stripe, and (d) zigzag reconstructed surfaces for 10 perovskites $A^{+}B^{5+}O_3$, $A^{2+}B^{4+}O_3$, and $A^{3+}B^{3+}O_3$. The green and blue bars schematically show the conduction and valence bands, respectively; only the inner edges of the bars, which correspond to the CBM and VBM with respect to the vacuum level (the negatives of the EAs and IPs), are meaningful, and the EA and IP values are shown in the figures. The broken and solid lines, respectively, indicate the experimentally reported values of the CBM and VBM with respect to the vacuum level.[62,87−92] The whole picture of the theoretical (e) CBM and (f) VBM relative to the vacuum level for the 4 reconstructed surfaces. The plus, cross, square, and diamond marks, respectively, denote the cation-exchange, checker, stripe, and zigzag reconstructed surface models.

$A^{2+}B^{4+}O_3$ and $A^{3+}B^{3+}O_3$ surfaces appear to be stabilized mainly by large $n_{surf}/n_{bulk}$ and $l_{surf}/l_{bulk}$ for cations $A$, lowering the Madelung surface energy (see Figure S3 in the Supporting Information for the correlation between $n_{surf}/n_{bulk}$ and $l_{surf}/l_{bulk}$ for cations $A$ and the Madelung surface energy).

We now turn to the tendency in the surface band positions. The scatter plots of $\varepsilon_{CBM}$ and $\varepsilon_{VBM}$ as a function of the relative coordination number ratio (RCNR) $\frac{n_{surf}^{A-O}/n_{bulk}^{A-O}}{n_{surf}^{B-O}/n_{bulk}^{B-O}}$ are shown in Figure 6. As a whole, negative correlations between the $\varepsilon_{CBM}$ or $\varepsilon_{VBM}$ and RCNR can be seen. We also found weak positive correlations between $\varepsilon_{VBM}$ and the Goldschmidt tolerance factor (see Figure S5 in the Supporting Information), which is similar to the trend of the half-$AO$-terminated surfaces (the stripe structures) of $A^{2+}B^{4+}O_3$.[66] On the other hand, correlations are unclear between $\varepsilon_{CBM}$ or $\varepsilon_{VBM}$ and total surface rumpling, as well as those between $\varepsilon_{CBM}$ and the Goldschmidt tolerance factor (see Figures S5 and S6 in the Supporting Information).

The case of RCNR < 1 (RCNR > 1) indicates that the coordination number of cation $A$ ($B$) at the surfaces decreases more drastically than that of cation $B$ ($A$) from the respective bulk values. In the region of RCNR < 1 (RCNR > 1), shallow (deep) $\varepsilon_{CBM}$ and $\varepsilon_{VBM}$ can be observed in all 4 surface structures and all 10 $ABO_3$ perovskites. These results indicate that shallow (deep) $\varepsilon_{CBM}$ and $\varepsilon_{VBM}$ are created by the drastic


https://doi.org/10.1021/acs.chemmater.2c03615
Chem. Mater. 2023, 35, 2047−2057

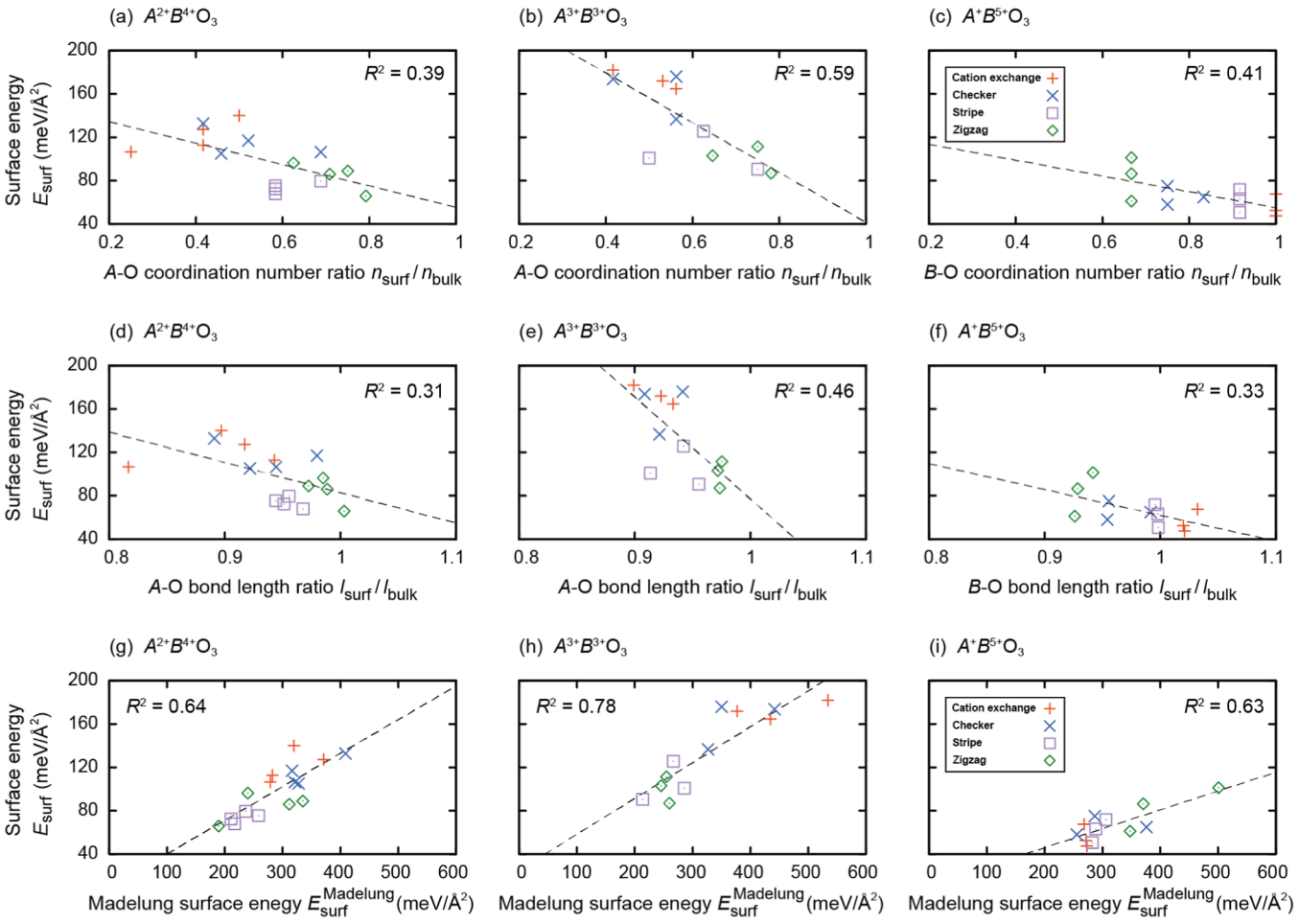


**Figure 5.** Surface energies against (a−c) coordination number ratio $n_{surf}/n_{bulk}$; (d−f) bond length ratio $l_{surf}/l_{bulk}$; and (g−i) Madelung surface energy for $A^{2+}B^{4+}O_3$, $A^{3+}B^{3+}O_3$, and $A^{+}B^{5+}O_3$. The plus, cross, square, and diamond marks, respectively, denote the cation-exchange, checker, stripe, and zigzag reconstructed surfaces. The dashed lines are the least-squares linear fittings, and the $R^2$ values denote their coefficients of determination.

decrease in the coordination number of cation $A$ ($B$) at the outermost surface layer. This chemical trend is consistent with the previous reports that fully $AO$-($BO_2$-)terminated surfaces have shallow (deep) $\varepsilon_{CBM}$ and $\varepsilon_{VBM}$.[63,66,86] Moreover, this discussion could be generalized in perovskites other than oxides as similar trends have been observed in halide perovskites such as $CH_3NH_3PbI_3$.[104,105]

## 3. CONCLUSIONS

Our evolutionary algorithm search has predicted the 4 types of reconstructed structures for the (001) nonpolar stoichiometric surfaces of $SrTiO_3$, $CaTiO_3$, $YAlO_3$, $LaAlO_3$, $NaTaO_3$, and $KTaO_3$. Using the 4 reconstructed surface structures, we systematically calculated the surface energies for 10 nonmetallic perovskite oxides and their EAs and IPs. We found that a driving force for the surface reconstruction is to regain the coordination numbers and bond lengths in the bulk phases as much as possible. As for $A^{2+}B^{4+}O_3$ and $A^{3+}B^{3+}O_3$, the fulfillment of the $A$-site coordination as much as possible at the surface lowers the surface energy, whereas that of the $B$-site coordination does for $A^{+}B^{5+}O_3$. Thus, the stripe and zigzag reconstructed structures are stabilized by regaining the $A$-site coordination for $A^{2+}B^{4+}O_3$ and $A^{3+}B^{3+}O_3$. The cation-exchange and checker reconstructed structures with significant rumpling are stabilized by regaining the $B$-site coordination for $A^{+}B^{5+}O_3$. Furthermore, we found negative correlations between $\varepsilon_{CBM}$ or $\varepsilon_{VBM}$ and the RCNR of cations $A$ and $B$, indicating that shallow (deep) band positions are created by the drastic decrease in the coordination number of cation $A$ ($B$) at the outermost layers. We believe that this study provides general insights into the surface reconstruction and band alignment of nonmetallic perovskite oxides.

## 4. COMPUTATIONAL METHODS

The first-principles calculations were carried out using the projector augmented-wave (PAW) method,[106] the Perdew−Burke−Ernzerhof functional tuned for solids (PBEsol) within the generalized gradient approximation,[107] and the Heyd−Scuseria−Ernzerhof (HSE06) hybrid functional with a Fock-exchange mixing parameter of 0.25 and a screening parameter of 0.208 Å$^{-1}$[108−110] as implemented in VASP.[111−113] The cutoff radii and valence electronic configurations of the PAW data sets used in the calculations are given in Table S2 in the Supporting Information. The PBEsol functional was used for bulk and surface geometry optimization, while the HSE06 hybrid functional was used to obtain more reliable band gaps and band-edge positions within the geometries determined using PBEsol. It has been reported that the HSE06 hybrid functional well reproduces the band gaps for a variety of semiconductors including perovskite oxides.[66,71,110,113,114] The Madelung energies with the formal charges were calculated by using the Ewald method as implemented in PYMATGEN.[115]

By using an *ab initio* evolutionary structure search method as implemented in AMADEUS,[116] the nonpolar stoichiometric (001) reconstructed surfaces were modeled for nonmetallic perovskites $A^{2+}B^{4+}O_3$, $A^{3+}B^{3+}O_3$, and $A^{+}B^{5+}O_3$ as follows: half coverages of the


https://doi.org/10.1021/acs.chemmater.2c03615
Chem. Mater. 2023, 35, 2047−2057

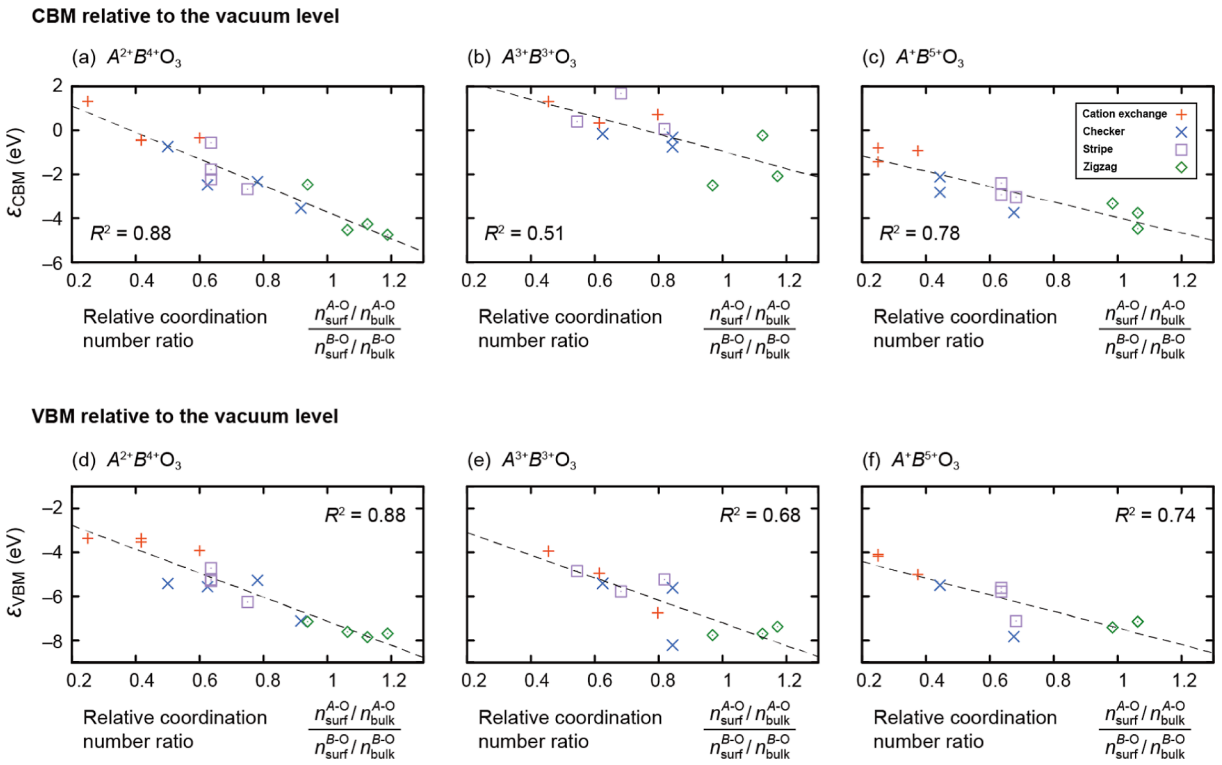


**Figure 6.** Relative coordination-number-ratio dependences of (a–c) CBM and (d–f) VBM relative to the vacuum level for $A^{2+}B^{4+}O_3$, $A^{3+}B^{3+}O_3$, and $A^{+}B^{5+}O_3$. The plus, cross, square, and diamond marks, respectively, denote the cation-exchange, checker, stripe, and zigzag reconstructed surfaces. The dashed lines are the least-squares linear fittings, and the $R^2$ values denote their coefficients of determination.

topmost layers were considered for 2 types of (001) surface supercells with different lateral periodicity units, $p(2 \times 2)$ and $p(\sqrt{2} \times 2\sqrt{2})$. Here, we describe the surface periodicity units of the orthorhombic phases based on a pseudo-cubic representation. Slab geometry with 6 layers was employed to reduce the computational cost for the reconstructed surface structure search. On one side of the slab, the topmost layer and the first sublayer were rearranged with the second sublayer relaxed and the other layers fixed (see Figure 1). The number of configurations was set to 30 in the population size of the conformational space annealing algorithm,[117] and the surface energy was used to express the objective function that describes specific target properties. The optimized outermost 2 layers are placed at both sides of the 13 subunit layers to construct slab models with a vacuum layer thicker than 14.8 Å for the subsequent surface energy and band position calculations. The lattice parameters were fixed at the corresponding relaxed bulk values. For the Brillouin zone integration, $k$-point sets were generated using $3 \times 3 \times 1$ and $4 \times 2 \times 1$ meshes for the $p(2 \times 2)$ and $p(\sqrt{2} \times 2\sqrt{2})$ supercells, respectively.

The EAs and IPs were evaluated using a standard procedure combining the energy levels of bulk and slab models through their electrostatic alignment.[66,118] Supporting Information includes refs 7, 8, 81, 84, and 119–122 and crystallographic data in the CIF format for our reconstructed surface structures.

## ■ ASSOCIATED CONTENT

### Supporting Information

The Supporting Information is available free of charge at https://pubs.acs.org/doi/10.1021/acs.chemmater.2c03615.

Total energy comparison between the 7 bulk polymorphs; surface energies of the 4 reconstructed surfaces as functions of $n_{surf}/n_{bulk}$ and $l_{surf}/l_{bulk}$; Madelung surface energies of the 4 reconstructed surfaces as functions of $n_{surf}/n_{bulk}$ and $l_{surf}/l_{bulk}$; cutoff-radius dependences of coordination numbers for cations $A$ and $B$ in bulk and outermost surfaces; Goldschmidt tolerance factor dependences of the band position for the 4 reconstructed surfaces; total surface rumpling dependences of the band position for the 4 reconstructed surfaces; cutoff radii and coordination numbers for the cations in $ABO_3$; cutoff radii and valence electronic configurations of the PAW data sets (PDF)

Crystallographic information files for the $ABO_3$ reconstructed surfaces (ZIP)

## ■ AUTHOR INFORMATION


### Corresponding Authors

**Yasuhide Mochizuki** − *Laboratory for Materials and Structures, Institute of Innovative Research, Tokyo Institute of Technology, Yokohama 226-8503, Japan;* Present Address: Department of Materials Science and Engineering, School of Materials and Chemical Technology, Tokyo Institute of Technology, 2-12-1 O-okayama, Meguro-ku, Tokyo 152-8550, Japan; orcid.org/0000-0002-8292-7736; Email: mochizuki.y.af@m.titech.ac.jp

**Fumiyasu Oba** − *Laboratory for Materials and Structures, Institute of Innovative Research, Tokyo Institute of Technology, Yokohama 226-8503, Japan;* orcid.org/0000-0001-7178-5333; Email: oba@msl.titech.ac.jp

### Authors

**Ha-Jun Sung** − *Laboratory for Materials and Structures, Institute of Innovative Research, Tokyo Institute of Technology, Yokohama 226-8503, Japan;* Present Address: Device Research Center, Samsung Advanced Institute and Technology, 130 Samsung-ro, Yeongtong-gu, Suwon, Gyeonggi-do 16678, South Korea.




https://doi.org/10.1021/acs.chemmater.2c03615
Chem. Mater. 2023, 35, 2047−2057

**Tomoya Gake** − *Laboratory for Materials and Structures, Institute of Innovative Research, Tokyo Institute of Technology, Yokohama 226-8503, Japan;* orcid.org/0000-0002-0788-6129

Complete contact information is available at: https://pubs.acs.org/10.1021/acs.chemmater.2c03615

### Notes

The authors declare no competing financial interest.

## ■ ACKNOWLEDGMENTS

The authors are grateful to Prof. Kee Joo Chang, Dr. In-Ho Lee, and Dr. Sunghyun Kim for allowing us to use the AMADEUS code. This work was supported by the JST CREST Grant no. JPMJCR17J2, JSPS KAKENHI Grant no. JP18J21747 and JP20H00302, and Design and Engineering by Joint Inverse Innovation for Materials Architecture project from MEXT. The computing resources of the Academic Center for Computing and Media Studies at Kyoto University and the Research Institute for Information Technology at Kyushu University were used for part of this work. VESTA[122] was used to draw Figure 1.

## ■ REFERENCES

(1) Haeni, J. H.; Irvin, P.; Chang, W.; Uecker, R.; Reiche, P.; Li, Y. L.; Choudhury, S.; Tian, W.; Hawley, M. E.; Craigo, B.; Tagantsev, A. K.; Pan, X. Q.; Streiffer, S. K.; Chen, L. Q.; Kirchoefer, S. W.; Levy, J.; Schlom, D. G. Room-temperature ferroelectricity in strained $SrTiO_3$. *Nature* **2004**, *430*, 758.

(2) Guo, J. W.; Wang, P. S.; Yuan, Y.; He, Q.; Lu, J. L.; Chen, T. Z.; Yang, S. Z.; Wang, Y. J.; Erni, R.; Rossell, M. D.; Gopalan, V.; Xiang, H. J.; Tokura, Y.; Yu, P. Strain-induced ferroelectricity and spin-lattice coupling in $SrMnO_3$ thin films. *Phys. Rev. B* **2018**, *97*, 235135.

(3) Sai, N.; Kolpak, A. M.; Rappe, A. M. Ferroelectricity in ultrathin perovskite films. *Phys. Rev. B: Condens. Matter Mater. Phys.* **2005**, *72*, 202101.

(4) Ederer, C.; Spaldin, N. A. Effect of epitaxial strain on the spontaneous polarization of thin film ferroelectrics. *Phys. Rev. Lett.* **2005**, *95*, 257601.

(5) Bousquet, E.; Dawber, M.; Stucki, N.; Lichtensteiger, C.; Hermet, P.; Gariglio, S.; Triscone, J.-M.; Ghosez, P. Improper ferroelectricity in perovskite oxide artificial superlattices. *Nature* **2008**, *452*, 732.

(6) Fu, D.; Taniguchi, H.; Itoh, M.; Koshihara, S.; Yamamoto, N.; Mori, S. Relaxor $Pb(Mg_{1/3}Nb_{2/3})O_3$: A ferroelectric with multiple inhomogeneities. *Phys. Rev. Lett.* **2009**, *103*, 207601.

(7) Oh, Y. S.; Luo, X.; Huang, F.-T.; Wang, Y.; Cheong, S.-W. Experimental demonstration of hybrid improper ferroelectricity and the presence of abundant charged walls in $(Ca,Sr)_3Ti_2O_7$ crystals. *Nat. Mater.* **2015**, *14*, 407.

(8) Yoshida, S.; Akamatsu, H.; Tsuji, R.; Hernandez, O.; Padmanabhan, H.; Sen Gupta, A. S.; Gibbs, A. S.; Mibu, K.; Murai, S.; Rondinelli, J. M.; Gopalan, V.; Tanaka, K.; Fujita, K. Hybrid Improper Ferroelectricity in $(Sr,Ca)_3Sn_2O_7$ and Beyond: Universal Relationship between Ferroelectric Transition Temperature and Tolerance Factor in $n = 2$ Ruddlesden-Popper Phases. *J. Am. Chem. Soc.* **2018**, *140*, 15690.

(9) Benedek, N. A.; Fennie, C. J. Hybrid improper ferroelectricity: A mechanism for controllable polarization-magnetization coupling. *Phys. Rev. Lett.* **2011**, *106*, 107204.

(10) Yoshida, S.; Fujita, K.; Akamatsu, H.; Hernandez, O.; Sen Gupta, A. S.; Brown, F. G.; Padmanabhan, H.; Gibbs, A. S.; Kuge, T.; Tsuji, R.; Murai, S.; Rondinelli, J. M.; Gopalan, V.; Tanaka, K. Ferroelectric $Sr_3Zr_2O_7$: Competition between Hybrid Improper Ferroelectric and Antiferroelectric Mechanisms. *Adv. Funct. Mater.* **2018**, *28*, 1801856.

(11) Nagai, T.; Shirakuni, H.; Nakano, A.; Sawa, H.; Moriwake, H.; Terasaki, I.; Taniguchi, H. Weak Ferroelectricity in $n = 2$ pseudo Ruddlesden-Popper-type. *Chem. Mater.* **2019**, *31*, 6257.

(12) Zhu, T.; Gibbs, A. S.; Benedek, N. A.; Hayward, M. A. Complex Structural Phase Transitions of the Hybrid Improper Polar Dion-Jacobson Oxides $RbNdM_2O_7$ and $CsNdM_2O_7$ (M = Nb, Ta). *Chem. Mater.* **2020**, *32*, 4340.

(13) Cascos, V. A.; Roberts-Watts, J.; Skingle, C.; Levin, I.; Zhang, W.; Halasyamani, P. S.; Stennett, M. C.; Hyatt, N. C.; Bousquet, E.; McCabe, E. E. Tuning between proper and hybrid-improper mechanisms for polar behavior in $CsLn_2Ti_2NbO_{10}$ Dion-Jacobson phases. *Chem. Mater.* **2020**, *32*, 8770.

(14) Zhang, B. H.; Xu, D.; Chen, B. H.; Liu, X. Q.; Hester, J. R.; Chen, X. M. Hybrid improper ferroelectricity in *A*-site cation ordered $Li_2La_2Ti_3O_{10}$ ceramic with triple-layer Ruddlesden−Popper structure. *Appl. Phys. Lett.* **2021**, *118*, 052903.

(15) Azuma, M.; Takata, K.; Saito, T.; Ishiwata, S.; Shimakawa, Y.; Takano, M. Designed Ferromagnetic, Ferroelectric $Bi_2NiMnO_6$. *J. Am. Chem. Soc.* **2005**, *127*, 8889.

(16) Liu, M.; Zhang, Y.; Lin, L.-F.; Lin, L.; Yang, S.; Li, X.; Wang, Y.; Li, S.; Yan, Z.; Wang, X.; Li, X.-G.; Dong, S.; Liu, J.-M. Direct observation of ferroelectricity in $Ca_3Mn_2O_7$ and its prominent light absorption. *Appl. Phys. Lett.* **2018**, *113*, 022902.

(17) Shirane, G.; Sawaguchi, E.; Takagi, Y. Dielectric Properties of Lead Zirconate. *J. Phys. Soc. Jpn.* **1951**, *6*, 208.

(18) Fu, D.; Endo, M.; Taniguchi, H.; Taniyama, T.; Itoh, M. $AgNbO_3$: A lead-free material with large polarization and electromechanical response. *Appl. Phys. Lett.* **2007**, *90*, 252907.

(19) Uppuluri, R.; Akamatsu, H.; Sen Gupta, A. S.; Wang, H.; Brown, C. M.; Agueda Lopez, K. E. A.; Alem, N.; Gopalan, V.; Mallouk, T. E. Competing Polar and Antipolar Structures in the Ruddlesden−Popper Layered Perovskite $Li_2SrNb_2O_7$. *Chem. Mater.* **2019**, *31*, 4418.

(20) Rao, C. N. R.; Ganguly, P.; Singh, K. K.; Ram, R. A. A comparative study of the magnetic and electrical properties of perovskite oxides and the corresponding two-dimensional oxides of $K_2NiF_4$ structure. *J. Solid State Chem.* **1988**, *72*, 14.

(21) Longo, J. M.; Raccah, P. M.; Goodenough, J. B. Magnetic Properties of $SrRuO_3$ and $CaRuO_3$. *J. Appl. Phys.* **1968**, *39*, 1327.

(22) Wang, J.; Neaton, J. B.; Zheng, H.; Nagarajan, V.; Ogale, S. B.; Liu, B.; Viehland, D.; Vaithyanathan, V.; Schlom, D. G.; Waghmare, U. V.; Spaldin, N. A.; Rabe, K. M.; Wuttig, M.; Ramesh, R. Epitaxial $BiFeO_3$ multiferroic thin film heterostructures. *Science* **2003**, *299*, 1719.

(23) Lee, J. H.; Fang, L.; Vlahos, E.; Ke, X.; Jung, Y. W.; Kourkoutis, L. F.; Kim, J.-W.; Ryan, P. J.; Heeg, T.; Roeckerath, M.; Goian, V.; Bernhagen, M.; Uecker, R.; Hammel, P. C.; Rabe, K. M.; Kamba, S.; Schubert, J.; Freeland, J. W.; Muller, D. A.; Fennie, C. J.; Schiffer, P.; Gopalan, V.; Johnston-Halperin, E.; Schlom, D. G. A strong ferroelectric ferromagnet created by means of spin-lattice coupling. *Nature* **2010**, *466*, 954.

(24) Müller, K. A.; Burkard, H. $SrTiO_3$: An intrinsic quantum paraelectric below 4 K. *Phys. Rev. B: Condens. Matter Mater. Phys.* **1979**, *19*, 3593.

(25) Samara, G. A.; Morosin, B. Anharmonic Effects in $KTaO_3$: Ferroelectric Mode, Thermal Expansion, and Compressibility. *Phys. Rev. B: Solid State* **1973**, *8*, 1256.

(26) Soon, H. P.; Taniguchi, H.; Itoh, M. Dielectric and soft-mode behaviors of $AgTaO_3$. *Phys. Rev. B: Condens. Matter Mater. Phys.* **2010**, *81*, 104105.

(27) Nagai, T.; Mochizuki, Y.; Shirakuni, H.; Nakano, A.; Oba, F.; Terasaki, I.; Taniguchi, H. Phase Transition from Weak Ferroelectricity to Incipient Ferroelectricity in $Li_2Sr(Nb_{1-x}Ta_x)_2O_7$. *Chem. Mater.* **2020**, *32*, 744.

(28) Schooley, J. F.; Hosler, W. R.; Cohen, M. L. Superconductivity in Semiconducting $SrTiO_3$. *Phys. Rev. Lett.* **1964**, *12*, 474.

(29) Lin, X.; Bridoux, G.; Gourgout, A.; Seyfarth, G.; Krämer, S.; Nardone, M.; Fauqué, B.; Behnia, K. Critical doping for the onset of a

two-band superconducting ground state in $SrTiO_{3-\delta}$. *Phys. Rev. Lett.* **2014**, *112*, 207002.
(30) Sleight, A. W.; Gillson, J. L.; Bierstedt, P. E. High-temperature superconductivity in the $BaPb_{1-x}Bi_xO_3$ system. *Solid State Commun.* **1975**, *17*, 27.
(31) Mattheiss, L. F.; Gyorgy, E. M.; Johnson, D. W., Jr. Superconductivity above 20 K in the Ba-K-Bi-O system. *Phys. Rev. B: Condens. Matter Mater. Phys.* **1988**, *37*, 3745.
(32) Itoh, M.; Sawada, T.; Kim, I.-S.; Inaguma, Y.; Nakamura, T. Electrical properties of the $A(Pb_{1-x}B_x)O_{3-\delta}$ ($A$ = Ba, Sr, $B$ = Sb, Bi) system. *Phys. C* **1992**, *204*, 194.
(33) Bednorz, J. G.; Muller, K. A. Possible High $T_c$ Superconductivity in the Ba-La-Cu-O System. *Z. Phys. B: Condens. Matter* **1986**, *64*, 189.
(34) Rischau, C. W.; Lin, X.; Grams, C. P.; Finck, D.; Harms, S.; Engelmayer, J.; Lorenz, T.; Gallais, Y.; Fauqué, B.; Hemberger, J.; Behnia, K. A ferroelectric quantum phase transition inside the superconducting dome of $Sr_{1-x}Ca_xTiO_{3-\delta}$. *Nat. Phys.* **2017**, *13*, 643.
(35) Maeno, Y.; Hashimoto, H.; Yoshida, K.; Nishizaki, S.; Fujita, T.; Bednorz, J. G.; Lichtenberg, F. Superconductivity in a layered perovskite without copper. *Nature* **1994**, *372*, 532.
(36) García-Muñoz, J. L.; Rodríguez-Carvajal, J.; Lacorre, P.; Torrance, J. B. Neutron-diffraction study of $RNiO_3$ ($R$ = La, Pr, Nd, Sm): Electronically induced structural changes across the metal-insulator transition. *Phys. Rev. B: Condens. Matter Mater. Phys.* **1992**, *46*, 4414.
(37) Torrance, J. B.; Lacorre, P.; Nazzal, A. I.; Ansaldo, E. J.; Niedermayer, C. Systematic study of insulator-metal transitions in perovskites $RNiO_3$ ($R$ = Pr, Nd, Sm, Eu) due to closing of charge-transfer gap. *Phys. Rev. B: Condens. Matter Mater. Phys.* **1992**, *45*, 8209.
(38) Alonso, J. A.; García-Muñoz, J. L.; Fernández-Díaz, M. T.; Aranda, M. A. G.; Martínez-Lope, M. J.; Casais, M. T. Charge Disproportionation in $RNiO_3$ Perovskites: Simultaneous Metal-Insulator and Structural Transition in $YNiO_3$. *Phys. Rev. Lett.* **1999**, *82*, 3871.
(39) Mercy, A.; Bieder, J.; Íñiguez, J.; Ghosez, P. Structurally triggered metal-insulator transition in rare-earth nickelates. *Nat. Commun.* **2017**, *8*, 1677.
(40) Goodenough, J. B. Covalency criterion for localized vs collective electrons in oxides with the perovskite structure. *J. Appl. Phys.* **1966**, *37*, 1415.
(41) Raccah, P. M.; Goodenough, J. B. First-Order Localized-Electron ⇆ Collective-Electron Transition in $LaCoO_3$. *Phys. Rev.* **1967**, *155*, 932.
(42) Kim, I.-S.; Itoh, M.; Nakamura, T. Electrical Conductivity and Metal-Nonmetal Transition in the Perovskite-Related Layered System $Ca_{n+1}Ti_nO_{3n+1-\delta}$ ($n$ = 2,3, and ∞). *J. Solid State Chem.* **1992**, *101*, 77.
(43) Taguchi, H.; Shimada, M. Metal-Insulator Transition in the System $(Ca_{1-x}La_x)MnO_{2.97}$ ($0.05 \leq x \leq 0.4$). *J. Solid State Chem.* **1986**, *63*, 290.
(44) Ohtomo, A.; Hwang, H. Y. A high-mobility electron gas at the $LaAlO_3/SrTiO_3$ heterointerface. *Nature* **2004**, *427*, 423.
(45) Reyren, N.; Thiel, S.; Caviglia, A. D.; et al. Superconducting Interfaces Between Insulating Oxides. *Science* **2007**, *317*, 1196.
(46) Tanaka, H.; Misono, M. Advances in designing perovskite catalysis. *Curr. Opin. Solid State Mater. Sci.* **2001**, *5*, 381.
(47) Labhasetwar, N.; Saravanan, G.; Kumar Megarajan, S. K.; Manwar, N.; Khobragade, R.; Doggali, P.; Grasset, F. Perovskite-type catalytic materials for environmental applications. *Sci. Technol. Adv. Mater.* **2015**, *16*, 036002.
(48) Hwang, J.; Rao, R. R.; Giordano, L.; Katayama, Y.; Yu, Y.; Shao-Horn, Y. Perovskites in catalysis and electrocatalysis. *Science* **2017**, *358*, 751.
(49) Kamata, K. Perovskite oxide catalysts for liquid-phase organic reactions. *Bull. Chem. Soc. Jpn.* **2019**, *92*, 133.
(50) Bashan, V.; Ust, Y. Perovskite catalysts for methane combustion: applications, design, effects for reactivity and partial oxidation. *Int. J. Energy Res.* **2019**, *43*, 7755.
(51) Polo-Garzon, F.; Wu, Z. Acid-base catalysis over perovskites: A review. *J. Mater. Chem. A* **2018**, *6*, 2877.
(52) Ou, Z.; Zhang, Z.; Qin, C.; Xia, H.; Deng, T.; Niu, J.; Ran, J.; Wu, C. Highly active and stable Ni/perovskite catalysts in steam methane reforming for hydrogen production. *Sustainable Energy Fuels* **2021**, *5*, 1845.
(53) Shoji, S.; Yin, G.; Nishikawa, M.; Atarashi, D.; Sakai, E.; Miyauchi, M. Photocatalytic reduction of $CO_2$ by $Cu_xO$ nanocluster loaded $SrTiO_3$ nanorod thin film. *Chem. Phys. Lett.* **2016**, *658*, 309.
(54) Shoji, S.; Peng, X.; Yamaguchi, A.; Watanabe, R.; Fukuhara, C.; Cho, Y.; Yamamoto, T.; Matsumura, S.; Yu, M.-W.; Ishii, S.; Fujita, T.; Abe, H.; Miyauchi, M. Photocatalytic uphill conversion of natural gas beyond the limitation of thermal reaction systems. *Nat. Catal.* **2020**, *3*, 148.
(55) Wang, K.; Han, C.; Shao, Z.; Qiu, J.; Wang, S.; Liu, S. Perovskite Oxide Catalysts for Advanced Oxidation Reactions. *Adv. Funct. Mater.* **2021**, *31*, 2102089.
(56) Nishiyama, H.; Yamada, T.; Nakabayashi, M.; Maehara, Y.; Yamaguchi, M.; Kuromiya, Y.; Nagatsuma, Y.; Tokudome, H.; Akiyama, S.; Watanabe, T.; Narushima, R.; Okunaka, S.; Shibata, N.; Takata, T.; Hisatomi, T.; Domen, K. Photocatalytic solar hydrogen production from water on a 100-$m^2$ scale. *Nature* **2021**, *598*, 304.
(57) Rondinelli, J. M.; May, S. J.; Freeland, J. W. Control of octahedral connectivity in perovskite oxide heterostructures: An emerging route to multifunctional materials discovery. *MRS Bull.* **2012**, *37*, 261.
(58) Mochizuki, Y.; Akamatsu, H.; Kumagai, Y.; Oba, F. Strain-engineered Peierls instability in layered perovskite $La_3Ni_2O_7$ from first principles. *Phys. Rev. Mater.* **2018**, *2*, 125001.
(59) Morita, K.; Davies, D. W.; Butler, K. T.; Walsh, A. Breaking the Aristotype: Featurization of Polyhedral Distortions in Perovskite Crystals. *Chem. Mater.* **2022**, *34*, 562.
(60) Schlom, D. G.; Chen, L.-Q.; Fennie, C. J.; Gopalan, V.; Muller, D. A.; Pan, X.; Ramesh, R.; Uecker, R. Elastic strain engineering of ferroic oxides. *MRS Bull.* **2014**, *39*, 118.
(61) Hosono, H. *Transparent Electronics: From Synthesis to Applications*; Wiley: New York, 2010.
(62) Robertson, J. Band offsets, Schottky barrier heights, and their effects on electronic devices. *J. Vac. Sci. Technol., A* **2013**, *31*, 050821.
(63) Stevanović, V.; Lany, S.; Ginley, D. S.; Tumas, W.; Zunger, A. Assessing capability of semiconductors to split water using ionization potentials and electron affinities only. *Phys. Chem. Chem. Phys.* **2014**, *16*, 3706.
(64) Scanlon, D. O.; Dunnill, C. W.; Buckeridge, J.; Shevlin, S. A.; Logsdail, A. J.; Woodley, S. M.; Catlow, C. R. A.; Powell, M. J.; Palgrave, R. G.; Parkin, I. P.; Watson, G. W.; Keal, T. W.; Sherwood, P.; Walsh, A.; Sokol, A. A. Band alignment of rutile and anatase $TiO_2$. *Nat. Mater.* **2013**, *12*, 798.
(65) Buckeridge, J.; Butler, K. T.; Catlow, C. R. A.; Logsdail, A. J.; Scanlon, D. O.; Shevlin, S. A.; Woodley, S. M.; Sokol, A. A.; Walsh, A. Polymorph Engineering of $TiO_2$: Demonstrating How Absolute Reference Potentials Are Determined by Local Coordination. *Chem. Mater.* **2015**, *27*, 3844.
(66) Sung, H.-J.; Mochizuki, Y.; Oba, F. Surface reconstruction and band alignment of nonmetallic $A(II)B(IV)O_3$ perovskites. *Phys. Rev. Mater.* **2020**, *4*, 044606.
(67) Ertl, G.; Knoezinger, H.; Weitkamp, J. *Handbook of Heterogeneous Catalysis*; Wiley-VCH: Weinheim, 1997.
(68) Soltani, S.; Hong, S.; Kim, B.; Kim, D.; Jung, J. K.; Sohn, B.; Noh, T. W.; Char, K.; Kim, C. $\sqrt{2}\times\sqrt{2}R45°$ surface reconstruction and electronic structure of $BaSnO_3$ film. *Phys. Rev. Mater.* **2020**, *4*, 055003.
(69) Franceschi, G.; Schmid, M.; Diebold, U.; Riva, M. Two-dimensional surface phase diagram of a multicomponent perovskite oxide: $La_{0.8}Sr_{0.2}MnO_3$ (110). *Phys. Rev. Mater.* **2021**, *5*, L092401.
(70) Ouhbi, H.; Aschauer, U. Water oxidation catalysis on reconstructed $NaTaO_3$ (001) surfaces. *J. Mater. Chem. A* **2019**, *7*, 16770.


https://doi.org/10.1021/acs.chemmater.2c03615
*Chem. Mater.* 2023, 35, 2047−2057

(71) Hinuma, Y.; Grüneis, A.; Kresse, G.; Oba, F. Band alignment of semiconductors from density-functional theory and many-body perturbation theory. *Phys. Rev. B: Condens. Matter Mater. Phys.* **2014**, *90*, 155405.
(72) Hinuma, Y.; Kumagai, Y.; Tanaka, I.; Oba, F. Effects of composition, crystal structure, and surface orientation on band alignment of divalent metal oxides: A first-principles study. *Phys. Rev. Mater.* **2018**, *2*, 124603.
(73) Hinuma, Y.; Gake, T.; Oba, F. Band alignment at surfaces and heterointerfaces of $Al_2O_3$, $Ga_2O_3$, $In_2O_3$, and related group-III oxide polymorphs: A first-principles study. *Phys. Rev. Mater.* **2019**, *3*, 084605.
(74) Traoré, B.; Basera, P.; Ramadan, A. J.; Snaith, H. J.; Katan, C.; Even, J. A Theoretical Framework for Microscopic Surface and Interface Dipoles, Work Functions, and Valence Band Alignments in 2D and 3D Halide Perovskite Heterostructures. *ACS Energy Lett.* **2022**, *7*, 349.
(75) Thapa, S.; Provence, S. R.; Jessup, D.; Lapano, J.; Brahlek, M.; Sadowski, J. T.; Reinke, P.; Jin, W.; Comes, R. B. Correlating surface stoichiometry and termination in $SrTiO_3$ films grown by hybrid molecular beam epitaxy. *J. Vac. Sci. Technol., A* **2021**, *39*, 053203.
(76) Deacon-Smith, D. E. E.; Scanlon, D. O.; Catlow, C. R. A.; Sokol, A. A.; Woodley, S. M. Interlayer Cation Exchange Stabilizes Polar Perovskite Surfaces. *Adv. Mater.* **2014**, *26*, 7252.
(77) Wang, Y.; Cheng, J.; Behtash, M.; Tang, W.; Luo, J.; Yang, K. First-principles studies of polar perovskite $KTaO_3$ surfaces: structural reconstruction, charge compensation, and stability diagram. *Phys. Chem. Chem. Phys.* **2018**, *20*, 18515.
(78) Enterkin, J. A.; Subramanian, A. K.; Russell, B. C.; Castell, M. R.; Poeppelmeier, K. R.; Marks, L. D. A homologous series of structures on the surface of $SrTiO_3$(110). *Nat. Mater.* **2010**, *9*, 245.
(79) Martirez, J. M. P.; Morales, E. H.; Saidi, W. A.; Bonnell, D. A.; Rappe, A. M. Atomic and Electronic Structure of the $BaTiO_3$ (001) $(\sqrt{5}\times\sqrt{5})$R26.6° Surface Reconstruction. *Phys. Rev. Lett.* **2012**, *109*, 256802.
(80) Lufaso, M. W.; Woodward, P. M. Prediction of the crystal structures of perovskites using the software program SPuDS. *Acta Crystallogr., Sect. B: Struct. Sci.* **2001**, *57*, 725.
(81) Tasker, P. W. The stability of ionic crystal surfaces. *J. Phys. C: Solid State Phys.* **1979**, *12*, 4977.
(82) Hinuma, Y.; Kumagai, Y.; Oba, F.; Tanaka, I. Categorization of surface polarity from a crystallographic approach. *Comput. Mater. Sci.* **2016**, *113*, 221.
(83) Zhao, X.; Selloni, A. Structure and stability of $NaTaO_3$(001) and $KTaO_3$(001) surfaces. *Phys. Rev. Mater.* **2019**, *3*, 015801.
(84) Setvin, M.; Reticcioli, M.; Poelzleitner, F.; Hulva, J.; Schmid, M.; Boatner, L. A.; Franchini, C.; Diebold, U. Polarity compensation mechanisms on the perovskite surface KTaO 3 (001). *Science* **2018**, *359*, 572.
(85) Vogt, J.; Weiss, H. The structure of NaCl(100) and KCl(100) single crystal surfaces: a tensor low energy electron diffraction analysis. *Surf. Sci.* **2001**, *491*, 155.
(86) Jacobs, R.; Booske, J.; Morgan, D. Understanding and Controlling the Work Function of Perovskite Oxides Using Density Functional Theory. *Adv. Funct. Mater.* **2016**, *26*, 5471.
(87) Mannhart, J.; Schlom, D. G. Oxide Interfaces — An Opportunity for Electronics. *Science* **2010**, *327*, 1607.
(88) Lin, J.; Hu, J.; Qiu, C.; Huang, H.; Chen, L.; Xie, Y.; Zhang, Z.; Lin, H.; Wang, X. In situ hydrothermal etching fabrication of $CaTiO_3$ on $TiO_2$ nanosheets with heterojunction effects to enhance $CO_2$ adsorption and photocatalytic reduction. *Catal. Sci. Technol.* **2019**, *9*, 336.
(89) Susaki, T.; Makishima, A.; Hosono, H. Work function engineering via $LaAlO_3/SrTiO_3$ polar interfaces. *Phys. Rev. B: Condens. Matter Mater. Phys.* **2011**, *84*, 115456.
(90) Xu, Y.; Schoonen, M. A. A. The absolute energy positions of conduction and valence bands of selected semiconducting minerals. *Am. Mineral.* **2000**, *85*, 543.
(91) Maarouf, A. A.; Gogova, D.; Fadlallah, M. M. Metal-doped $KNbO_3$ for visible light photocatalytic water splitting: A first principles investigation. *Appl. Phys. Lett.* **2021**, *119*, 063901.
(92) Edalati, K.; Fujiwara, K.; Takechi, S.; Wang, Q.; Arita, M.; Watanabe, M.; Sauvage, X.; Ishihara, T.; Horita, Z. Improved Photocatalytic Hydrogen Evolution on Tantalate Perovskites $CsTaO_3$ and $LiTaO_3$ by Strain-Induced Vacancies. *ACS Appl. Energy Mater.* **2020**, *3*, 1710.
(93) Ueda, K.; Yanagi, H.; Noshiro, R.; Hosono, H.; Kawazoe, H. Vacuum ultraviolet reflectance and electron energy loss spectra of $CaTiO_3$. *J. Phys.: Condens. Matter* **1998**, *10*, 3669.
(94) van Benthem, K.; Elsässer, C.; French, R. H. Bulk electronic structure of $SrTiO_3$: Experiment and theory. *J. Appl. Phys.* **2001**, *90*, 6156.
(95) Robertson, J. Band offsets of wide-band-gap oxides and implications for future electronic devices. *J. Vac. Sci. Technol., B: Microelectron. Nanometer Struct.–Process., Meas., Phenom.* **2000**, *18*, 1785.
(96) Zhydachevskyy, Y.; Hizhnyi, Y.; Nedilko, S. G.; Kudryavtseva, I.; Pankratov, V.; Stasiv, V.; Vasylechko, L.; Sugak, D.; Lushchik, A.; Berkowski, M.; Suchocki, A.; Klyui, N. Band Gap Engineering and Trap Depths of Intrinsic Point Defects in $RAlO_3$ (R = Y, La, Gd, Yb, Lu) Perovskites. *J. Phys. Chem. C* **2021**, *125*, 26698.
(97) Ogisu, K.; Ishikawa, A.; Shimodaira, Y.; Takata, T.; Kobayashi, H.; Domen, K. Electronic Band Structures and Photochemical Properties of La−Ga-based Oxysulfides. *J. Phys. Chem. C* **2008**, *112*, 11978.
(98) Diao, C. L.; Zheng, H. W. The preparation and surface photovoltage characterization of $KNbO_3$ powder. *J. Mater. Sci.: Mater. Electron.* **2015**, *26*, 3108.
(99) Kato, H.; Kudo, A. Water Splitting into $H_2$ and $O_2$ on Alkali Tantalate Photocatalysts $ATaO_3$ (A = Li, Na, and K). *J. Phys. Chem. B* **2001**, *105*, 4285.
(100) Hanzawa, K.; Iimura, S.; Hiramatsu, H.; Hosono, H. Material Design of Green-Light-Emitting Semiconductors: Perovskite-Type Sulfide $SrHfS_3$. *J. Am. Chem. Soc.* **2019**, *141*, 5343.
(101) Yoshida, S.; Akamatsu, H.; Hayashi, K. Electronic Origin of Non-Zone-Center Phonon Condensation: Octahedral Rotation as a Case Study. *Phys. Rev. Lett.* **2021**, *127*, 215701.
(102) Waroquiers, D.; Gonze, X.; Rignanese, G.-M.; Welker-Nieuwoudt, C.; Rosowski, F.; Göbel, M.; Schenk, S.; Degelmann, P.; André, R.; Glaum, R.; Hautier, G. Statistical analysis of coordination environments in Oxides. *Chem. Mater.* **2017**, *29*, 8346.
(103) Levine, J. D.; Mark, P. Theory and Observation of Intrinsic Surface States on Ionic Crystals. *Phys. Rev.* **1966**, *144*, 751.
(104) Quarti, C.; De Angelis, F. D.; Beljonne, D. Influence of Surface Termination on the Energy Level Alignment at the $CH_3NH_3PbI_3$ Perovskite/C60 Interface. *Chem. Mater.* **2017**, *29*, 958.
(105) Mirzehmet, A.; Ohtsuka, T.; Abd Rahman, S. A. A.; Yuyama, T.; Krüger, P.; Yoshida, H. Surface Termination of Solution-Processed $CH_3NH_3PbI_3$ Perovskite Film Examined using Electron Spectroscopies. *Adv. Mater.* **2021**, *33*, 2004981.
(106) Blöchl, P. E. Projector augmented-wave method. *Phys. Rev. B: Condens. Matter Mater. Phys.* **1994**, *50*, 17953.
(107) Perdew, J. P.; Ruzsinszky, A.; Csonka, G. I.; Vydrov, O. A.; Scuseria, G. E.; Constantin, L. A.; Zhou, X.; Burke, K. Restoring the Density-Gradient Expansion for Exchange in Solids and Surfaces. *Phys. Rev. Lett.* **2008**, *100*, 136406.
(108) Heyd, J.; Scuseria, G. E.; Ernzerhof, M. Hybrid functionals based on a screened coulomb potential. *J. Chem. Phys.* **2003**, *118*, 8207.
(109) Heyd, J.; Scuseria, G. E.; Ernzerhof, M. Erratum: Hybrid functionals based on a screened Coulomb potential. *J. Chem. Phys.* **20032006**, *124*, 219906.
(110) Krukau, A. V.; Vydrov, O. A.; Izmaylov, A. F.; Scuseria, G. E. Influence of the exchange screening parameter on the performance of screened hybrid functionals. *J. Chem. Phys.* **2006**, *125*, 224106.


https://doi.org/10.1021/acs.chemmater.2c03615
*Chem. Mater.* 2023, 35, 2047−2057

(111) Kresse, G.; Furthmüller, J. Efficient iterative schemes for ab initio total-energy calculations using a plane-wave basis set. *Phys. Rev. B: Condens. Matter Mater. Phys.* **1996**, *54*, 11169.
(112) Kresse, G.; Joubert, D. From ultrasoft pseudopotentials to the projector augmented-wave method. *Phys. Rev. B: Condens. Matter Mater. Phys.* **1999**, *59*, 1758.
(113) Paier, J.; Marsman, M.; Hummer, K.; Kresse, G.; Gerber, I. C.; Ángyán, J. G. Screened hybrid density functionals applied to solids. *J. Chem. Phys.* **2006**, *124*, 154709.
(114) Hinuma, Y.; Hatakeyama, T.; Kumagai, Y.; Burton, L. A.; Sato, H.; Muraba, Y.; Iimura, S.; Hiramatsu, H.; Tanaka, I.; Hosono, H.; Oba, F. Discovery of earth-abundant nitride semiconductors by computational screening and high-pressure synthesis. *Nat. Commun.* **2016**, *7*, 11962.
(115) Ong, S. P.; Richards, W. D.; Jain, A.; Hautier, G.; Kocher, M.; Cholia, S.; Gunter, D.; Chevrier, V. L.; Persson, K. A.; Ceder, G. Python Materials Genomics (pymatgen): A robust, open-source python library for materials analysis. *Comput. Mater. Sci.* **2013**, *68*, 314.
(116) Lee, I.-H.; Oh, Y. J.; Kim, S.; Lee, J.; Chang, K. J. Ab initio materials design using conformational space annealing and its application to searching for direct band gap silicon crystals. *Comput. Phys. Commun.* **2016**, *203*, 110.
(117) Lee, J.; Lee, I.-H.; Lee, J. Unbiased Global Optimization of Lennard-Jones Clusters for n ≤ 201 Using the Conformational Space Annealing Method. *Phys. Rev. Lett.* **2003**, *91*, 080201.
(118) Oba, F.; Kumagai, Y. Design and exploration of semiconductors from first principles: A review of recent advances. *Appl. Phys. Express* **2018**, *11*, 060101.
(119) Mochizuki, Y.; Nagai, T.; Shirakuni, H.; Nakano, A.; Oba, F.; Terasaki, I.; Taniguchi, H. Coexisting Mechanisms for Ferroelectric Phase Transition in $Li_2SrNb_2O_7$. *Chem. Mater.* **2021**, *33*, 1257.
(120) Zhang, B. H.; Liu, X. Q.; Chen, X. M. Review of experimental progress of hybrid improper ferroelectricity in layered perovskite oxides. *J. Phys. D: Appl. Phys.* **2022**, *55*, 113001.
(121) Goldschmidt, V. M. Die Gesetze der Krystallochemie. *Naturwissenschaften* **1926**, *14*, 477.
(122) Momma, K.; Izumi, F. VESTA 3 for three-dimensional visualization of crystal. *J. Appl. Crystallogr.* **2011**, *44*, 1272.

## Recommended by ACS

**Intercalation Chemistry of the Disordered Rocksalt $Li_3V_2O_5$ Anode from Cluster Expansions and Machine Learning Interatomic Potentials**

Xingyu Guo, Shyue Ping Ong, *et al.*
FEBRUARY 10, 2023
CHEMISTRY OF MATERIALS
READ

**Tunable Magnetic Transition Temperatures in Organic–Inorganic Hybrid Cobalt Chloride Hexagonal Perovskites**

Teresa Lee, Robert J. Cava, *et al.*
FEBRUARY 15, 2023
CHEMISTRY OF MATERIALS
READ

**B-Site Columnar-Ordered Halide Double Perovskites: Breaking Octahedra Motions Induces Strong Lattice Anharmonicity and Thermal Anisotropy**

Qi Wang, Yue Chen, *et al.*
FEBRUARY 09, 2023
CHEMISTRY OF MATERIALS
READ

**Enhanced Thermoelectric Properties of $Zr_{0.85-x}Hf_xNb_{0.15-y}Ta_yCoSb$ Medium-Entropy Alloys: Tradeoff between "What to Alloy" and "How Much to Al...**

Rongchun Chen, Tongmin Wang, *et al.*
FEBRUARY 28, 2023
CHEMISTRY OF MATERIALS
READ

**Get More Suggestions >**


https://doi.org/10.1021/acs.chemmater.2c03615
*Chem. Mater.* 2023, 35, 2047−2057